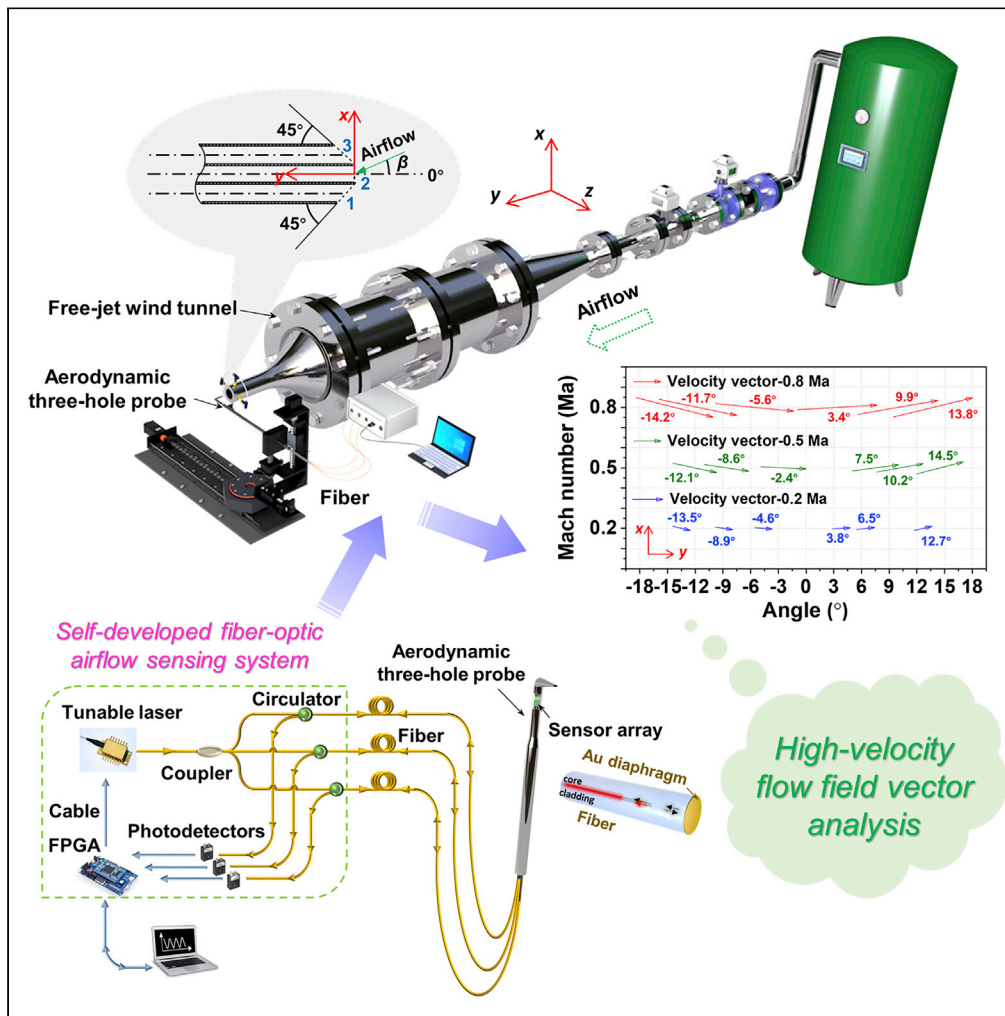**CellPress**

Article

Fiber-optic integrated aerodynamic three-hole vector probe for high-velocity flow field measurement

Yueying Liu, Zhenguo Jing, Qiang Liu, ..., Fu Tian, Rui Li, Wei Peng

jingzg@dlut.edu.cn

Highlights

Real-time measurement of high-velocity flow field vector

Batch fabrication of miniature fiber-optic tip pressure sensors using MEMS technology

Self-developed fiber-optic multichannel white light interferometry interrogator

Feasibility verification of fiber-optic sensing system for flow field analysis

iScience

Article

Fiber-optic integrated aerodynamic three-hole vector probe for high-velocity flow field measurement

Yueying Liu,[1] Zhenguo Jing,[2,4,*] Qiang Liu,[2] Ang Li,[1] Wenwen Li,[3] Sen Zhang,[1] Ang Lee,[2] Fu Tian,[3] Rui Li,[2] and Wei Peng[2]

SUMMARY

An integrated aerodynamic three-hole pressure probe (THP) based on a fiber-optic tip sensor array for high-velocity flow field vector measurement is developed and demonstrated in wind tunnel testing. The sensor array consisting of three miniature pressure fiber-tip sensors is integrated into three pressure conduits inside top area of the THP, which serves to mitigate pneumatic pressure loss and is expected for a more reliable analysis of flow characteristics. Fast real-time data acquisition is implemented by a compact self-developed multichannel white light interferometry (WLI) interrogator. Well-calibrated maps of the fiber-optic THP are developed in a subsonic free-jet wind tunnel to derive the velocity vectors in a yaw angular range of $\pm 15°$ at Mach numbers of 0.2 Ma ($\sim$70 m/s), 0.5 Ma ($\sim$170 m/s), and 0.8 Ma ($\sim$300 m/s) while related flow characteristics are analyzed. This work is desired to provide a potential candidate for turbomachinery experimental investigation in fluid mechanics community.

INTRODUCTION

The development of high-pressure compressors and turbines has always played a pivotal role in the modern aeroengine manufacturing industry (Royce, 2015; Backman and Williams, 1992). The turbomachinery, however, as a key component of the aeroengine, faces great challenges in the design process due to its harsh operating environment and complex flow field conditions (Uzol and Katz, 2007). The interaction of rotating and non-rotating components in turbomachinery, secondary flows, or blade wakes shedding usually induces highly fluctuating flow fields. Sources of the non-constancy have to be understood by some technical means before designing turbomachines. The magnitude and direction of the velocity fields within the turbomachinery environments may present important variations over a certain timescale and help to explain the characteristics of the flow fields. With the development and optimization of computational fluid dynamics (CFD), some flow regimes can be learned numerically (Wang et al., 2014), but the experimental investigation is still of interest for the scientific community and industrial fields. Experiments on turbomachinery occupy an important position in obtaining the compressor cascade performance as well as propeller blade flow, etc. (Zachos et al., 2011; Ragni et al., 2011). Measurement techniques and instrumentation have been proposed for turbomachinery applications, either non-intrusively or intrusively, including particle image velocimetry (PIV) (Westerweel et al., 2013), laser Doppler velocimetry (LDV) (Li et al., 2019), laser two-focus method (L2F) (Mousavi and Fahimeh, 2020), hot-wire anemometry (HWA) (Bailey et al., 2010), and multi-hole pressure probes (MHPs) (Heckmeier et al., 2019; Telionis et al., 2009; Argüelles Díaz et al., 2009; Crowder et al., 1997). In turbomachinery measurements, the lack of sufficient optical access prevents the use of PIV, LDV, and L2F which are mainly driven by free-space optical techniques. Moreover, the absence of adequate mechanical robustness and vulnerability to gas contamination are also issues for HWA.

MHPs, so-called fast-response aerodynamic probes (FRAPs), are known for offering reasonable cost, good repeatability, and durable gauging techniques that readily adapt to both turbomachinery environments (Heckmeier et al., 2019) and flight testing (Telionis et al., 2009). It serves the purpose of extracting the velocity components in magnitude and direction in an airstream by reading the port pressures. Using an MHP that has been appropriately calibrated in a known flow field, the velocity vector can be extracted by acquiring the port-pressure readings and comparing them with the calibration maps (Argüelles Díaz et al., 2009). Thus, the precise measurements of pressure and correct plotting of calibration maps are

[1]School of Optoelectronic Engineering and Instrumentation Science, Dalian University of Technology, Dalian 116024, China

[2]School of Physics, Dalian University of Technology, Dalian 116024, China

[3]School of Energy and Power Engineering, Dalian University of Technology, Dalian 116024, China

[4]Lead contact

*Correspondence: jingzg@dlut.edu.cn

crucial to realizing velocity vector analysis with high accuracy. Port pressures derived from the MHFs are traditionally guided by pressure tubes and then measured through the connection of remote pressure transducers, which may lead to the problems of pneumatic loss, long response time, and low efficiency (Crowder et al., 1997). When the airflow passes through a long transmission distance, internal fluid friction and wall friction generate a portion of energy loss due to the presence of viscous drag, intuitively expressed as pressure loss or pressure drop (White, 2011; Anderson, 2010). It eventually results in the issues of measurement inaccuracy (Andersen and Binder, 1967; Tropea et al., 2007). To reduce the pneumatic transmission distances, the transducers in a few studies are mounted in close proximity to the ports of MHPs, thereby acquiring some accurate pressure fluctuations and more reliable flow field information (Gossweiler et al., 1995; Johansen et al., 2003; Schettini et al., 2018).

An aerodynamic cylindrical probe topped with piezoresistive Wheatstone bridge type pressure sensor chips was developed by Gossweiler et al. to confirm the rapid decay from impeller outflow of a radial compressor (Gossweiler et al., 1995). Johansen et al. embedded a micro-electro-mechanical system (MEMS) sensor array in the head of an MHP to resolve the instantaneous velocity vector (Johansen et al., 2003). Schettini et al. designed a smart probe for flow angles measurements where five pressure transducers welded on a specific PCB are housed in the probe to sense the pressure at the tip ports (Schettini et al., 2018). However, these electronic pressure transducers are deficient in terms of electromagnetic interference and miniaturization for sensing sizes. Fiber-optic sensors are expected to transcend the limitations of traditional electronic transducers and become new alternatives, thanks to their distinctive merits such as small size, geometrical flexibility, ease of distribution and networking, and immunity to most electromagnetic distortion (Zou et al., 2021; Bai et al., 2020; Liu et al., 2016; Lawson et al., 2016; Cipullo et al., 2012). Some recent developments on fiber-optic flow sensors have focused on the measurement of the velocity magnitude in the airflow field. Examples include fiber-optic anemometers based on dual-channel Fabry-Perot (FP) interferometers (Wang et al., 2019), as well as a single-channel differential-pressure FP sensor and a diaphragm-based sensor with built-in fiber Bragg Grating (FBGs), both coupled for use with Pitot tubes (Liu et al., 2020b; Fujiwara et al., 2020). There are also precedents expecting to combine fiber-optic pressure sensors with MHPs for future wind tunnel applications, such as multiple MEMS optical transducers (Zhou and Sheplak, 2020) and differentially dynamic FP pressure sensors (Heckmeier et al., 2019). And the development of new MHPs based on fiber-optic sensing technology for more reliable measurement of flow field vectors remains a continuous research topic.

In this paper, a miniaturized aerodynamic three-hole pressure probe (THP) based on a fiber-optic tip sensor array for high-velocity flow field vector measurements has been successfully applied in a subsonic free-jet wind tunnel. The sensor array consisting of three miniature pressure fiber-tip sensors is integrated into three pressure conduits inside the top area of the probe to construct a miniaturized aerodynamic THP. Using the integrated aerodynamic THP with a built-in fiber-optic tip sensor array, the pressure measurements of the airstream will occur right at the top area of the probe rather than flowing through long pressure tubes to reach the sensors. The design serves to mitigate pneumatic pressure loss caused by the viscous drag of the airflow over long transmission distances, promising high-precision calibration and more reliable measurements of the flow field. Furthermore, the minimization of flow disturbances created by intrusive probes is also very important for the accurate measurement of flow field parameters. Miniature ultra-thin circular gold diaphragms manufactured mainly from MEMS technology form the basic pressure sensing units of the fiber-tip sensors in the sensor array, while helping to create sensing structures with an outer diameter (OD) of just ~125 μm. The smaller size of the single fiber-tip sensor benefits the miniaturization of the aerodynamic THP top area, thereby reducing intrusive perturbation to the testing airflow field and facilitating the exploration of actual flow. And the high uniformity of the gold sensing diaphragms produced by the MEMS manufacturing process is also a key factor in supporting simultaneous and consistent response as well as stable operation of the three fiber-tip sensors in practical velocity vector and related flow field characteristics studies of applied turbomachinery community. Fast real-time data from the sensor array are acquired by a compact self-developed multi-channel white light interferometry (WLI) interrogator consisting of a modulated grating Y-branch (MG-Y) tunable laser, a field-programmable gate array (FPGA) control and acquisition module, and three photodetectors (PDs). And the calibration map plotting and velocity vector measurements are implemented at Mach numbers of about 0.2 Ma (~70 m/s), 0.5 Ma (~170 m/s), and 0.8 Ma (~300 m/s) in a flow yaw angular range of ±15° while other related flow characteristics are also analyzed. With the advantages of probe miniaturization, high acquisition and demodulation rates, and large measurable range, the

fiber-optic integrated aerodynamic THP offers potential application value for pneumatic turbomachinery studies in most electromagnetic interference environments.

RESULTS AND DISCUSSION

Aerodynamic THP geometry and sensor integration

Although a variety of MHPs have been devised for decomposition of the flow velocity vector and related flow characteristics measurement in turbine components, THPs are still the most well known and widely used. THPs are frequently made up of a streamlined axisymmetric body pointing to the airflow field and used for two-dimensional (2D) flow fields. As the name implies, it features three pressure sensing ports. Similar to the Pitot tube, it also works by the stagnation of the flow around the probe when inserted into any flow field (Tropea et al., 2007). The pressure distribution around the surface of the THP tip can be described as the maximum pressure at the stationary point and the lower pressure at other surrounding points. It indicates that the pressure at specific points on the tip surface can be related to the direction and magnitude of the flow velocity. Based on the conservation of energy, the stagnation/total pressure P_0 at the stationary point can be expressed as the sum of static pressure P_s and the dynamic pressure P_d when the mechanical loss is ignored (White, 2011; Tropea et al., 2007)

$$P_0 = P_s + P_d = P_s + \frac{1}{2}\rho U_\infty^2 \qquad \text{(Equation 1)}$$

where U_∞ is the flow velocity in the free stream, and ρ (kg/m^3) is the density of the fluid.

Thus, the surface pressure of the THP tip is usually sampled at three points to determine the direction and magnitude of 2D flow field vector. Through experimental and empirical analysis, and long-term evolution in the field of aerodynamics, the three locations are typically designed on the axis of the probe tip and at two equally spaced points on both sides of the probe tip surface (Argüelles Díaz et al., 2010; Díaz, 2003). When the flow velocity vector is perpendicular to the central pressure port on the probe tip surface, that point gives the conventional stagnation/total pressure. The yaw direction can be inferred by relating the differential pressure between the symmetrical pressure side ports to the inflow velocity vector through proper calibration (Argüelles Díaz et al., 2009, 2010; Díaz, 2003). And the flow velocity magnitude can be inferred from the subsequent data processing.

Generally, the port pressures of traditional THPs are transmitted to remote pressure transducers via long pressure tubes of even several meters in length to explore the velocity vectors of airflow fields, which may result in pneumatic pressure loss. Without considering complex local loss, the pressure loss during the test often originates from the loss along the path caused by the viscous friction of the fluid flowing in the pipeline. The pneumatic pressure loss can be estimated by (White, 2011; Anderson, 2010)

$$P_{loss} = \left(\alpha \frac{l}{d}\right)\rho \frac{v^2}{2} \qquad \text{(Equation 2)}$$

where P_{loss}, α, l, d, and v (m/s) are pressure loss, coefficient of frictional drag along the path, length of the round pressure tube, the inner diameter (ID) of the tube, and the flow velocity, respectively. According to Equation 2, the pressure loss increases with the increasing transmission distance for the same airflow environment, which may eventually lead to unreliable aerodynamic analysis.

To mitigate the pneumatic pressure loss and improve response performance, the sensor array is integrated near the pressure ports. The structure of the designed fiber-optic integrated aerodynamic THP is shown schematically in Figure 1. The aerodynamic THP is composed mainly of an external stainless steel housing, three internal stainless steel thin pressure conduits, and an integrated fiber-optic tip pressure sensor array, as shown in Figures 1A and 1D. The aerodynamic THP has an oval-like construction at the tip of the probe. Port 2 is centrally located and Port 1 and Port 3 are arranged symmetrically on either side, both at an angle of 45° with respect to Port 2, as shown in Figure 1B. The long axis of this oval is approximately 2.3 mm and the short axis is about 1.0 mm. The OD of the pressure ports is 0.6 mm while the ID is 0.4 mm. The integrated sensor array near the probe tip of the aerodynamic THP serves to measure the port pressure values. Each pressure fiber-tip sensor in the sensor array with an OD of ~125 μm and a sensing area length of ~160 μm is embedded into a thin pressure conduit that is welded to the pressure port. And the cylindrical housing encasing the thin pressure conduits has an OD of about 3 mm at the top area of the aerodynamic THP. The above components form the most forward area of the aerodynamic THP in contact with the airflow field.
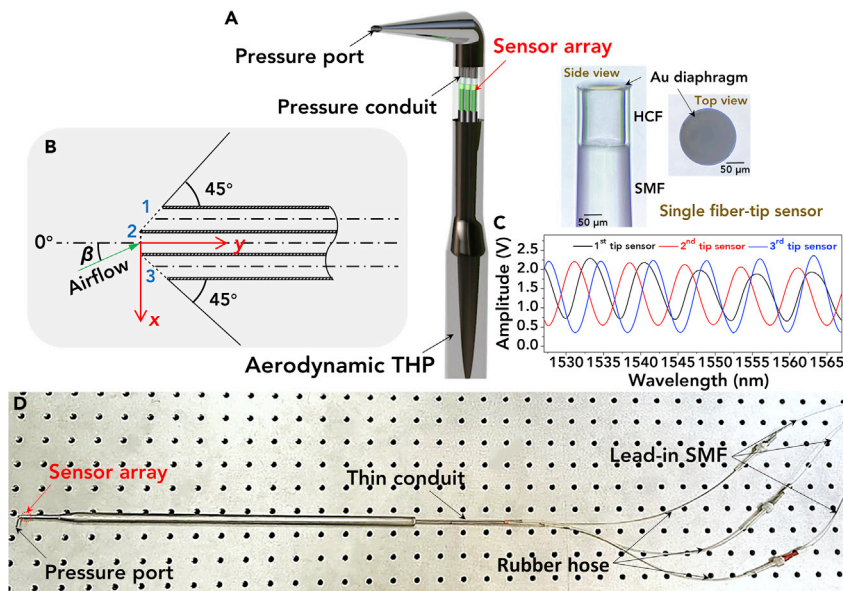
Figure 1. Structure, angular definition, and interference spectra of the fiber-optic integrated aerodynamic THP
(A) The schematic diagram of the fiber-optic integrated aerodynamic THP.
(B) Angular definition.
(C) The spectra of the fiber-optic tip pressure sensor array.
(D) The image of a typical aerodynamic THP.

The lead-in single-mode fibers (SMFs, 9 μm/125 μm, YOFC) pass through the thin conduits and are connected to the self-developed multichannel WLI interrogator. The interference spectra of the pressure sensor array are shown in Figure 1C.

Moreover, the magnitude of the port pressures is closely related to the yaw angle β of the airflow. The flow angular definition of the proposed fiber-optic integrated aerodynamic THP is shown in Figure 1B. The angle defined between the probe axis and the velocity vector v is the yaw angle β, the pitch angle is considered to be 0 in the 2D plane. When the β-angle of the input airflow is positive, the pressure value derived from Port 3 is considered to be higher than the one from Port 1. At this point, Port 1 is regarded to deviate more from the streamline than Port 3. Proper calibration in a known flow field is essential for correct data output from THPs, and the interpolated calibration maps are available throughout their lifetime unless the geometry of the probes has changed (Azartash-Namin, 2017). Well-calibrated THPs can be inserted into an unknown flow field, where the port pressures are recorded and compared with interpolated calibration maps to determine the velocity vector and related flow characteristics. When using the THPs for decomposing the flow velocity vector, the velocity components v_x and v_y are related to the yaw angle β as

$$v_x = - v \cdot \sin \beta \qquad \text{(Equation 3)}$$
$$v_y = v \cdot \cos\beta \qquad \text{(Equation 4)}$$

Sensor design and principle

During the testing, the integrated pressure sensor array of the developed aerodynamic THP will respond to the pressures from the three ports. Side and top views of a typical single fiber-tip sensor in the sensor array under an optical microscope are shown in Figure 1A. To minimize the size of the sensor, ultra-thin circular gold diaphragms with a thickness of ~250 nm and a diameter of ~125 μm are prepared by MEMS lithography and wet etching to form the basic pressure sensing units of the fiber-tip sensors, as shown in Figure 2. Firstly, a glass substrate is ultrasonically cleaned in acetone, isopropanol, and deionized (DI) water for five minutes, respectively. A thin film of gold (thickness of ~250 nm) is deposited on the cleaned glass substrate by magnetron sputtering (Q300TD, Quorum Technologies). The positive photoresist (S1805, Shipley) is spin coated onto the gold film and soft baked at 90°C for 1 min. After exposure with photolithography equipment and immersion in a developer solution, the developed substrate is etched with a mixture of iodine, potassium iodide, and DI water in a mass ratio of 1:5:100 (I_2:KI:H_2O) to form the shape of gold
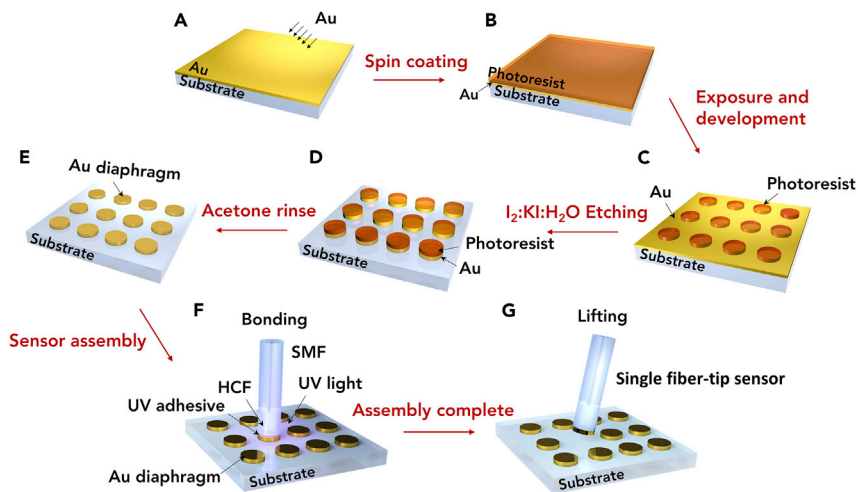
Figure 2. Fabrication process of a typical single fiber-optic tip pressure sensor
(A) Deposit gold film.
(B) Spin coat positive photoresist.
(C) Exposure and development.
(D) Wet etch with I_2:KI:H_2O.
(E) Remove photoresist.
(F) Sensor assembly.
(G) Assembly complete.

sensing diaphragms. Then, the etched substrate is rinsed with acetone to remove the photoresist. As shown in Figure 1A, the formed gold diaphragms have uniform shapes and high surface flatness. The entire MEMS manufacturing process is clean and efficient, producing hundreds of well-shaped diaphragms at a time.

Thereafter, a hollow-core fiber (HCF, 80 μm/125 μm, FiberHome) that fused at the endface of the SMF is cut to a specified length of ~160 μm under an optical microscope. The HCF endface dipped with UV adhesive (3311, Loctite) is aligned with a gold sensing diaphragm. Exposed to UV irradiation, the UV adhesive between the HCF and the gold diaphragm is cured, joining the two interfaces together, as shown in Figure 2. Owing to the poor adherence of gold film to glass (Pask and Fulrath, 1962), the gold diaphragm prepared directly on the common glass substrate is easily peeled off by the endface of HCF coated with UV adhesive. Finally, the sensor array consisting of three fiber-tip sensors is integrated into the head of the aerodynamic THP near the pressure ports, where the pressure measurements of the airstream will occur right at the top area of the probe to mitigate the problems of pressure loss.

The miniature fiber-optic tip sensor array inside the pressure conduits serves to measure the pressure introduced by the three ports of the developed aerodynamic THP. Each single fiber-tip sensor in the sensor array can be regarded as a low-finesse diaphragm-based FP interferometer (DFPI), where the two reflections can be estimated by a two-beam interferometric model. The interference spectrum can be expressed as an intensity-modulated signal

$$I = I_1 + I_2 + 2\sqrt{I_1 I_2}\cos\left(\frac{4\pi nL}{\Lambda} + \pi\right)$$

(Equation 5)

where I is the intensity of the interference spectrum, I_1 and I_2 are intensities of the two reflections, n is the refractive index of the medium filled in FP cavity, L is the FP cavity length, Λ is the working wavelength, and π is the additional phase of half-wave loss.

The main pressure sensing element of a single fiber-tip sensor is made by the gold diaphragm, with Young's modulus E of 79.5 GPa and Poisson's ratio μ of 0.42. When the sensing diaphragm is exposed to external pressure, the circular diaphragm deforms, resulting in FP cavity length variations, which can be determined by (Giovanni, 1982)

$$\Delta L = \frac{3(1 - \mu^2)r^4}{16Eh^3} \Delta P \qquad \text{(Equation 6)}$$

where P is the applied pressure, r and h are the effective radius and thickness of the sensing diaphragm, respectively.

Each single fiber-tip sensor in the pressure sensor array has a linear measurable range, which can be described as (Giovanni, 1982)

$$P_{\text{linear}} = \frac{8Eh^4}{5(1 - \mu^2)r^4} \qquad \text{(Equation 7)}$$

With the effective radius of the diaphragm being 40 μm and the thickness being ~250 nm, the theoretical linear sensitivity of the fiber-tip sensor is about 318.25 nm/kPa. And the linear pressure measurable range is about 0–235.66 Pa. Beyond this linear range, a nonlinear response interval may be reached at high Mach numbers (or high wind pressure). But the three FP cavity lengths can still respond to the three pressure values within the elastic deformation range of the gold diaphragms and as functions of wind pressure.

Calibration of aerodynamic THP

Experimental calibration for an aerodynamic THP can be implemented in a known flow field using the probe rotation method. The THP is first inserted vertically into a closed wind tunnel (Roux, 2004) or a free jet (Gossweiler et al., 1995) so that Port 2 is aligned with the direction of the airstream, and Port 1 and Port 3 are symmetrical with respect to the flow direction. The yaw angle of the THP at this position is defined as 0°. The pressure from Port 2 is equal to the total pressure of the airflow, while the pressure from Port 1 is similar to that from Port 3. The THP rotates in the airflow field and is calibrated in certain angular steps over a range of yaw angles at different Mach number environments, depending on the required accuracy and measurement range. The pressure values introduced from the three ports of the aerodynamic THP are related to the flow characteristics, such as velocity vector, yaw angle, total pressure, static pressure, and density of the airflow field. The extensive calibration data for the aerodynamic THP can be simplified and exploited by using dimensionless calibration coefficients, which are defined below

$$K_\beta = \frac{P_3 - P_1}{(P_2 - P_1) + (P_2 - P_3)} \qquad \text{(Equation 8)}$$

$$K_0 = \frac{P_0 - P_2}{(P_2 - P_1) + (P_2 - P_3)} \qquad \text{(Equation 9)}$$

$$K_{13} = \frac{P_1 - P_3}{P_0 - P_s} \qquad \text{(Equation 10)}$$

$$KK_1 = \frac{P_2 - P_1}{P_0 - P_s} \qquad \text{(Equation 11)}$$

$$KK_3 = \frac{P_2 - P_3}{P_0 - P_s} \qquad \text{(Equation 12)}$$

where P_1, P_2, P_3, P_0, and P_s are the pressure values from Port 1, Port 2, and Port 3 of the aerodynamic THP, total pressure, and static pressure of the flow field, respectively. K_β is yaw angle coefficient of the airflow, K_0 is total pressure coefficient, K_{13}, KK_1, and KK_3 correspond to static pressure coefficients. And the above coefficients can be obtained by measuring P_1, P_2, P_3, P_0, and P_s in a known flow field.

These non-dimensional calibration coefficients at multiple yaw angles and different Mach number environments are calculated as the basis for the interpolated calibration maps. The calibration maps are generally plotted as a trend of the calibration coefficients varying with yaw angles (Rautenberg et al., 2019). Then, the well-calibrated aerodynamic THP will be placed in an unknown flow field to collect the same data for comparison with the calibration maps during the flow measurements. For velocity vector reconstruction and related flow characteristics analysis in an unknown airflow field, the pressure data at each test point are acquired by the well-calibrated aerodynamic THP as P_1, P_2, and P_3. Via calculating the present K_β based on Equation 8 and substituting it into the prior interpolated calibration curves for this coefficient, the yaw angle β can be known. Thus, the present K_0, K_{13}, KK_1, and KK_3 can be obtained by the substitution of β into the interpolation curves of the corresponding coefficients. And the total pressure P_0 will be determined according to Equation 9. Similarly, the static pressure P_s can be calculated through Equations 10–12 when β and P_0 are available. It is worth mentioning that P_s is analyzed by utilizing the three static pressure coefficients curves (K_{13}, KK_1, and KK_3) simultaneously to minimize some potential calculation errors. At certain yaw

angles, situations where the pressure values measured by the two ports of the probe are similar may exist, resulting in small differential pressure. This is detrimental to the inverse calculation of P_s based on Equations 10–12, because the very small numerator might magnify the error. Therefore, the static pressure in various angle intervals is analyzed by employing different static pressure coefficient curves depending on the measuring situation.

Furthermore, the accurate calculation of total pressure P_0 and static pressure P_s is very important for the reliable solution of the following velocity magnitude and density of the airflow field. The velocity coefficient λ, or dimensionless velocity, is often adopted to study the high-velocity flow of gases, which is related to flow velocity v and critical sound velocity c_{cr} (m/s) (Anderson, 2010; Tropea et al., 2007)

$$\lambda = \frac{v}{c_{cr}} \qquad \text{(Equation 13)}$$

The velocity coefficient can be obtained from an aerodynamic function that describes the ratio of the static parameters of the airflow to the total parameters (Anderson, 2010; Tropea et al., 2007)

$$\pi(\lambda) = \frac{P_s}{P_0} = \left(1 - \frac{\gamma - 1}{\gamma + 1}\lambda^2\right)^{\frac{\gamma}{\gamma - 1}} \qquad \text{(Equation 14)}$$

where γ is the adiabatic index, generally 1.40 for dry air. In adiabatic flow, the critical sound velocity c_{cr} is a constant related only to the total temperature of the airstream, which can be determined by (Anderson, 2010; Tropea et al., 2007)

$$c_{cr} = \sqrt{\frac{2}{\gamma + 1}\gamma R T_0} \qquad \text{(Equation 15)}$$

where T_0 (K) is the temperature at the stationary point of $v = 0$ and is referred to as the total temperature.

Besides, according to the ideal gas equation of state in aerodynamics, the density of the airflow can also be derived and approximated as (Anderson, 2010; Tropea et al., 2007)

$$\rho = \frac{P_a + P_s}{R T_0} \qquad \text{(Equation 16)}$$

where P_a is the atmospheric pressure, and R is the ideal gas constant (R = 287.058 J/(kg·K) for dry air).

Calibration of the fiber-optic integrated aerodynamic THP in free jet

Before using the developed fiber-optic integrated aerodynamic THP in the experimental calibration, the relationship between the FP cavity lengths of the sensor array and applied pressure should be determined. The experimental setup for the fiber-optic tip pressure sensor array combined with the self-developed multi-channel WLI interrogator is shown in Figure 3. The top area of the aerodynamic THP integrated
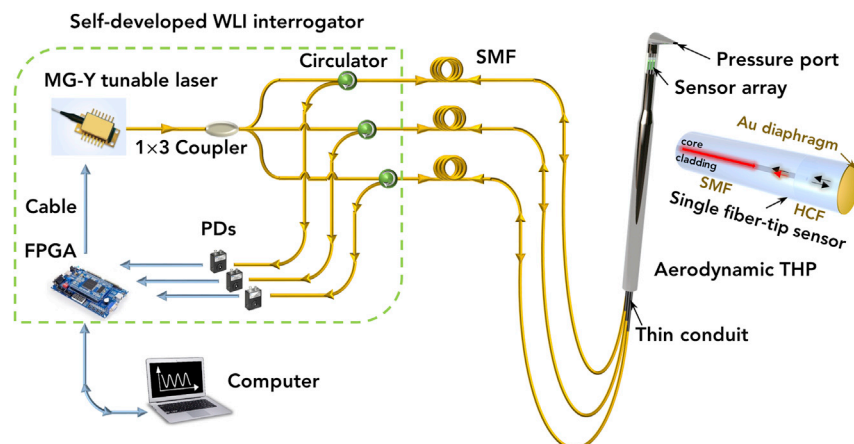
Figure 3. Experimental setup for the fiber-optic integrated aerodynamic THP combined with the compact self-developed multichannel WLI interrogator
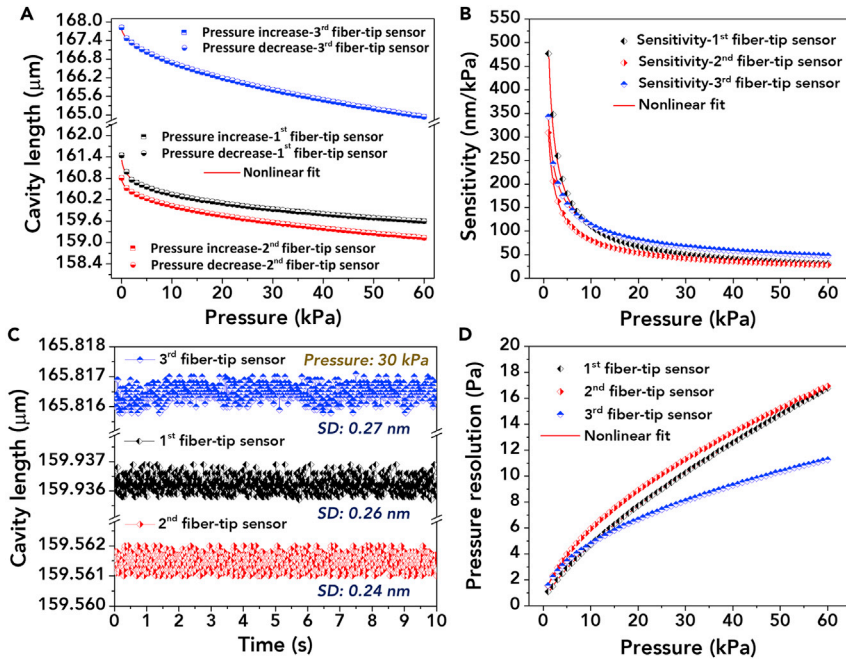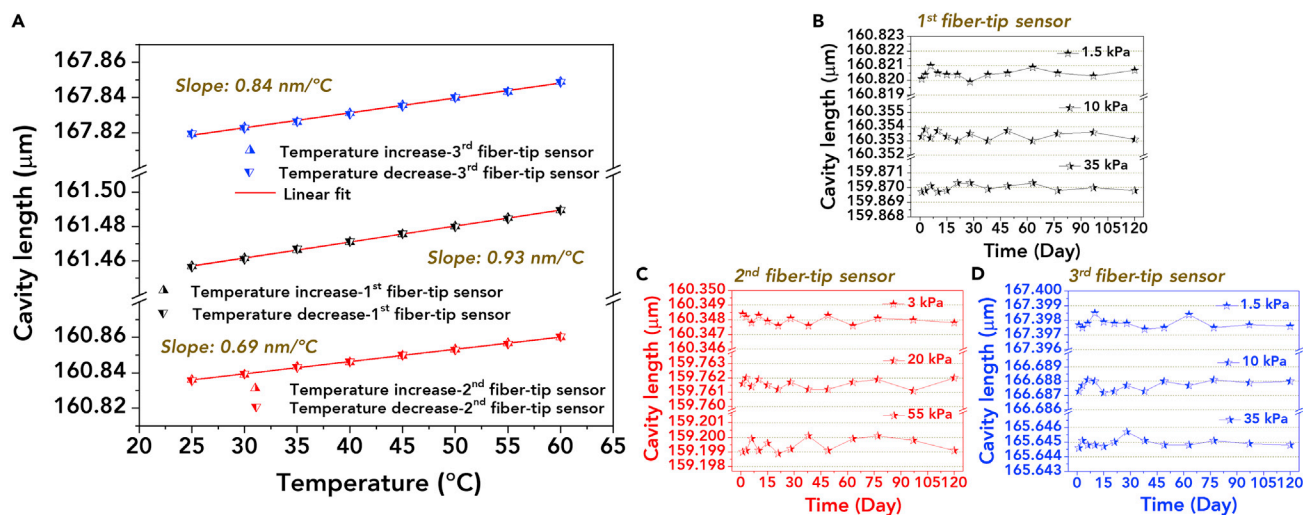
Figure 4. The pressure response characteristics of the fiber-optic tip pressure sensor array
(A) The nonlinear response of the sensor array between FP cavity lengths and applied pressure from 0 to 60 kPa.
(B) Sensitivity variations of the sensor array with the changes of the applied pressure.
(C) The evaluation of SDs in a 10-s time span at 30 kPa.
(D) Resolution variations of the sensor array with the changes of the applied pressure.

with the sensor array is encapsulated in a pressure chamber and the internal pressure is supplied by a pressure generator (113A, ConST). Real-time data acquisition and processing are realized by the self-developed multichannel WLI interrogator, mainly consisting of a broadly tunable MG-Y laser, an FPGA, and three PDs. The MG-Y tunable laser (ATLS7500, AOC Technologies), one of the Vernier tuned distributed Bragg reflector (VT-DBR) lasers, is employed as the light source. The output wavelength is controlled by injection currents of three sections: the right reflection section (I_{RR}), the left reflection section (I_{LR}), the phase section (I_{PH}), and the output intensity is adjusted by fine-tuning the injection current of the semiconductor optical amplifier (I_{SOA}) section (O'Connor et al., 2008; Liu et al., 2021; Liu et al., 2019). Full-spectrum wavelength scanning of the MG-Y laser at an interval of 8 pm from 1527 nm to 1567 nm and synchronized data acquisition with a frequency of 100 Hz are both implemented by the FPGA, and the output intensity of each wavelength is adjusted to a consistent 10.5 dBm. The output interference spectra of the fiber-tip sensors in the sensor array when no wind pressure is applied are shown in Figure 1C. The spectra are simultaneously processed by the cross-correlation signal processing method (Jing, 2006; Han et al., 2004; Xie et al., 2015) and the demodulated length of the three FP cavities can be expressed as functions of applied pressure. The initial cavity lengths of the three fiber-tip sensors in the sensor array corresponding to Port 1, Port 2, and Port 3 are measured to be about 161.457 μm, 160.836 μm, and 167.819 μm, respectively.

Figure 4A shows the response of the pressure sensor array after an increase/decrease pressure cycle in the range of 0–60 kPa (1 kPa per step). During the pressure increasing cycle, the FP cavity lengths decrease with the increasing pressure because of the sensing diaphragms' deformation. As the pressure decreases, the FP cavity lengths recover and return to their original state at the zero point. The variations of the FP cavity lengths with applied pressure mainly exhibit nonlinear response since most of the applied pressure is beyond the linear measurable range. Fitted with power function curves, the pressure calibration equations of the sensor array can be expressed as

$$\begin{cases} L_1 = 161.457 - 0.566P^{0.290} \\ L_2 = 160.836 - 0.309P^{0.416} \\ L_3 = 167.819 - 0.341P^{0.521} \end{cases}$$ (Equation 17)

Figure 5. The temperature response characteristics, repeatability, and long-term stability of the fiber-optic tip pressure sensor array

(A) Temperature response from room temperature 25°C to 60°C.

(B) FP cavity length variations of the 1st fiber-tip sensor under pressure conditions of 1.5 kPa, 10 kPa, and 35 kPa over 120 days.

(C) FP cavity length variations of the 2nd fiber-tip sensor under pressure conditions of 3 kPa, 20 kPa, and 55 kPa over 120 days.

(D) FP cavity length variations of the 3rd fiber-tip sensor under pressure conditions of 1.5 kPa, 10 kPa, and 35 kPa over 120 days.

Owing to the nonlinear variations, the sensitivities of the pressure sensor array also vary with the changes of the applied pressure. As shown in Figure 4B, sensitivities decrease as the applied pressure rises, with a maximum sensitivity of 477.03 nm/kPa and a minimum sensitivity of 28.33 nm/kPa. The pressure resolutions of the three fiber-tip sensors can be evaluated by measuring the standard deviations (SDs) of the FP cavity lengths (Liu et al., 2020a; Zhou et al., 2019). In Figure 4C, the changes of the FP cavity lengths are recorded at a steady pressure of 30 kPa over a 10-s time span, where the SDs are approximately 0.26 nm, 0.24 nm, and 0.27 nm, respectively. The resolution of the FP cavity length is usually calculated at twice the SD, and the pressure resolutions of the three fiber-tip sensors vary with the sensitivities, from the highest resolution of 1.09 Pa (0.0018% F.S.) to the lowest one of 16.94 Pa (0.028% F.S.) (F.S., 0–60 kPa), as shown in Figure 4D.

Although the fiber-tip sensors target wind pressure measurements in the free jet of the wind tunnel, they are also subject to temperature effects to some extent. The temperature response of the pressure sensor array from room temperature 25°C to 60°C is investigated in a temperature control box, as shown in Figure 5A. The three fiber-tip sensors exhibit linear responses to temperature, where the temperature sensitivities are 0.93 nm/°C, 0.69 nm/°C, and 0.84 nm/°C, respectively. The crosstalk is principally caused by the thermal expansion of the main components constituting the fiber-tip sensors, such as HCFs, air trapped in FP cavities, and UV adhesive layers when the surrounding temperature changes. Therefore, the pressure and temperature responses of fiber-tip sensors need to be calibrated before the practical wind tunnel testing. Besides, the temperature of the free jet in the wind tunnel generally does not raise drastic variations over the testing time due to the presence of automatic control systems. Such error is considered acceptable in these applications with limited temperature variations. Otherwise, the effective temperature compensation mechanism, such as cascaded with an FBG temperature sensor in our related work (Zhou et al., 2019; Wang et al., 2012; Jing et al., 2018), is required to eliminate the crosstalk between temperature and wind pressure. In future work, some materials with better thermal stability and other adhesive-free fabrication processes will also be considered for sensor assembly to reduce the impact of material mismatch (Liu et al., 2020a; Wang et al., 2010, 2012).

The repeatability and long-term stability of the sensor array are also important metrics to be discussed during the application. The pressure calibration for wind pressure simulated environments with free jet of 0.2 Ma, 0.5 Ma, and 0.8 Ma when the yaw angle of the fiber-optic integrated aerodynamic THP is 0 is exemplified in Figures 5B–5D. The results show that the FP cavity lengths do not change significantly at room temperature and are in good agreement with the pressure calibration equation of the sensor array (Equation 17). The miniature pressure fiber-tip sensors assembled from gold diaphragms, HCFs,
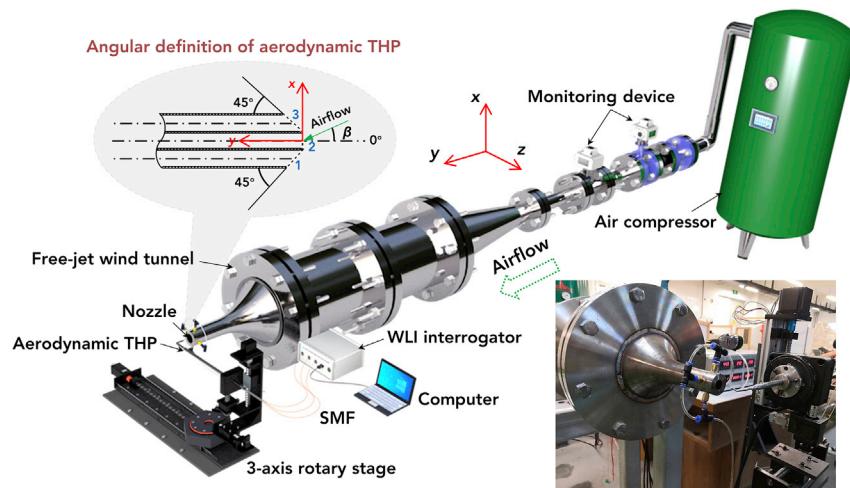
Figure 6. Schematic diagram of the experimental setup and angular definition for the fiber-optic integrated aerodynamic THP calibration process in a continuous subsonic free-jet wind tunnel

and UV adhesive have proven to offer good repeatability and measurement stability over a long period of time, ensuring a service life of at least several months.

The aerodynamic THP requires prior calibration under known flow conditions before it can be applied to explore velocity vectors and related flow characteristics in unknown airflow fields. The experimental setup for the calibration process of the fiber-optic integrated aerodynamic THP within a continuous subsonic wind tunnel is depicted in Figure 6. The experimental calibration is performed in the open free-jet wind tunnel, as placing the probe to be calibrated in a conventional closed wind tunnel test area may produce large blockage errors (Wyler, 1975). An air compressor controlled by a variable-frequency drive (VFD) generates a steady airflow with high Mach numbers. The free jet discharges out through a circular outlet. The throat diameter of the converging nozzle is 20 mm. The developed fiber-optic integrated aerodynamic THP is mounted on a computer-controlled 3-axis rotary stage with the tip of the probe positioned at 30 mm from the nozzle. The pressure ports at the tip of the aerodynamic THP are adjusted by the 3-axis rotary stage placed in the center of the free jet and face the incoming flow. The first step is to determine where the incidence angle of the airflow is 0°. The tip of the aerodynamic THP is rotated until Port 2 faces the streamline and Port 1 and Port 3 are symmetrical with respect to the flow streamline. At this moment, $P_2 = P_0$, and $P_1 \approx P_3$. After determining the measurement point at 0°, the calibration testing starts by rotating the aerodynamic THP to an angular position of 15°. Then, the calibration process of the fiber-optic integrated aerodynamic THP is implemented at different Mach numbers of about 0.2 Ma (~70 m/s), 0.5 Ma (~170 m/s), and 0.8 Ma (~300 m/s) with an interval of 1° in the angle varying range of 15°~−15°, respectively. The atmospheric pressure of the experimental environment P_a is measured by the monitoring device to be 100.43 kPa, and the corresponding total temperatures T_0 of the three airflow fields with three Mach numbers above are 25.4°C, 31.7°C, and 35.2°C, respectively.

The output interference spectra of the pressure sensor array integrated in the aerodynamic THP are recorded in a yaw angular range from 15° to −15° at Mach number environments of 0.2 Ma, 0.5 Ma, and 0.8 Ma. The variations in the spectra of the three fiber-tip sensors in the yaw angles of 15°, 10°, 5°, 0°, −5°, −10°, and −15° at a Mach number environment of 0.5 Ma are exemplified in Figure 7. The spectrum of the 1st fiber-tip sensor is blue-shifted with the changes of yaw angle from 15° to −15° in Figure 7A, while the one of the 2nd fiber-tip sensor changes slightly with yaw angles and the one of the 3rd fiber-tip sensor is red-shifted with the yaw angles in Figures 7B and 7C, respectively. The spectra also exhibit similar variations at Mach numbers of 0.2 Ma and 0.8 Ma. The output interference spectra are simultaneously processed by the cross-correlation signal processing method to get the values of FP cavity lengths (Jing, 2006; Han et al., 2004; Xie et al., 2015).
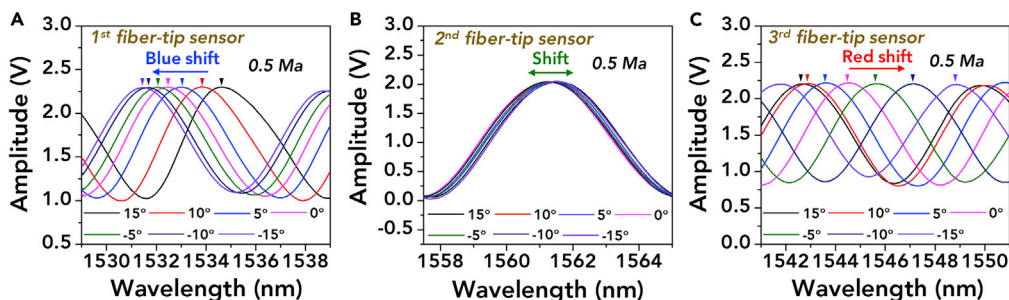
Figure 7. The shift in the output interference spectra of the fiber-optic tip pressure sensor array in the yaw angles of 15°, 10°, 5°, 0°, −5°, −10°, and −15° at a Mach number of 0.5 Ma
(A) The 1ˢᵗ fiber-tip sensor.
(B) The 2ⁿᵈ fiber-tip sensor.
(C) The 3ʳᵈ fiber-tip sensor.

Figure 8A shows the FP cavity length variations throughout the testing and visualizes the entire test process. The pressure sensor array exhibits simultaneous response and good consistency. When the free jet starts to discharge out in each Mach number environment of 0.2 Ma, 0.5 Ma, and 0.8 Ma, the airflow begins to contact the gold sensing diaphragms and causes the deformation, exhibiting dramatic reduction in the
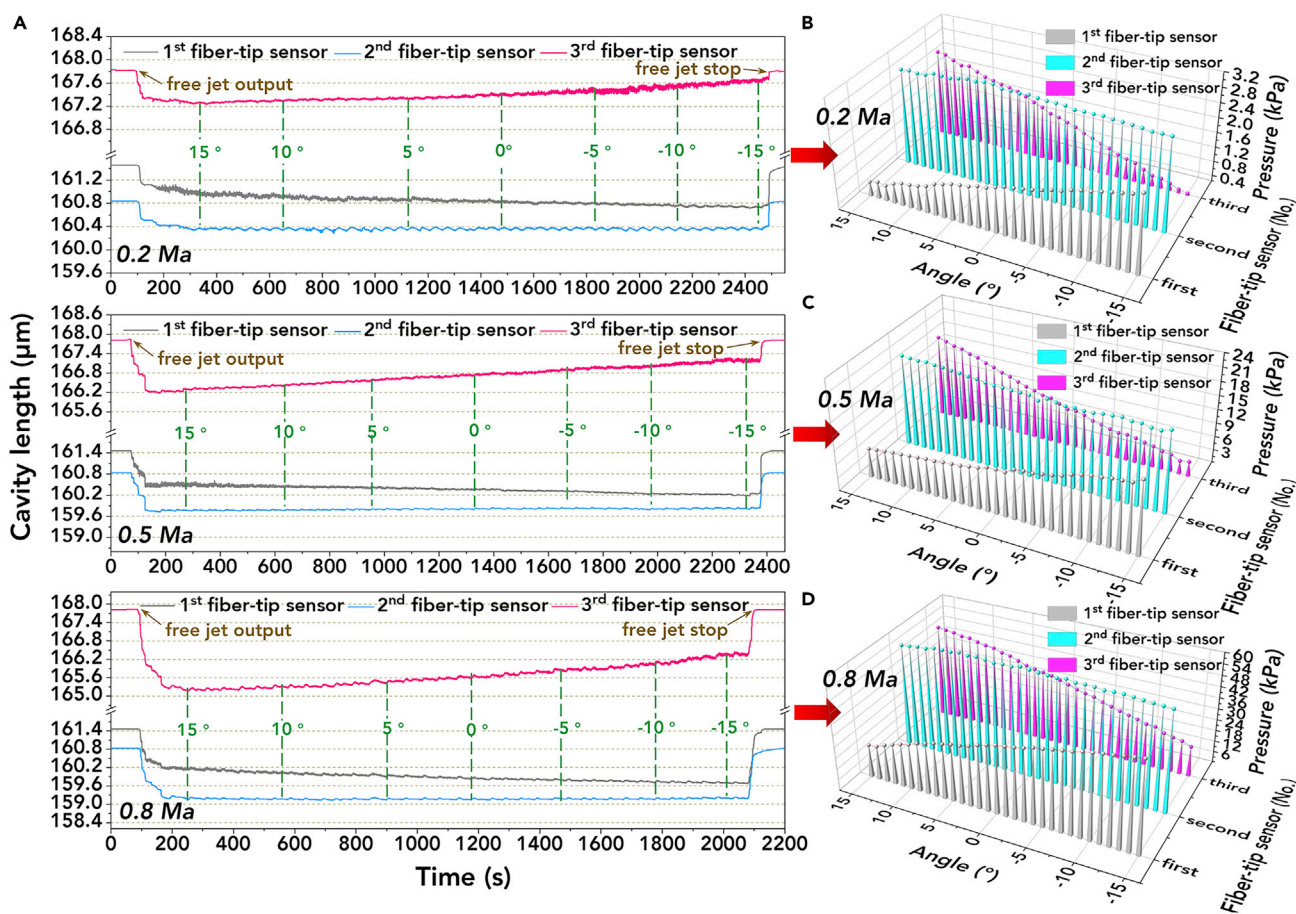
Figure 8. Responses of the fiber-optic tip pressure sensor array in a yaw angular range from 15° to −15° at Mach number environments of 0.2 Ma, 0.5 Ma, and 0.8 Ma throughout the whole testing process
(A) FP cavity length variations.
(B)–(D) Real-time port pressures on average.
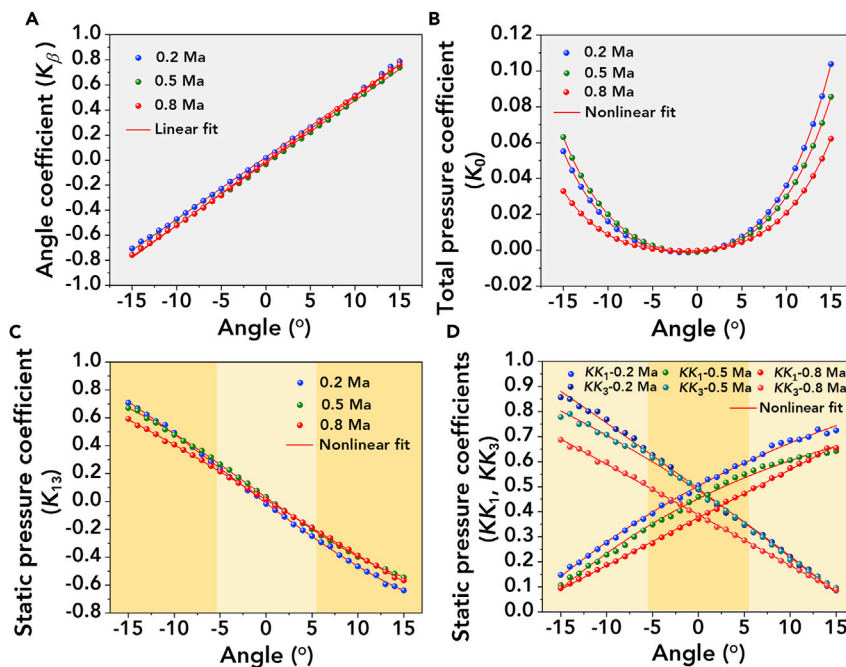
Figure 9. Dimensionless calibration coefficient curves within ±15° yaw angle variations for flow field characterization

(A) Yaw angle coefficient K_β.

(B) Total pressure coefficient K_0.

(C) Static pressure coefficient K_{13}.

(D) Static pressure coefficients KK_1 and KK_3.

lengths of the three FP cavities. Then, the three FP cavity lengths become stable after the airflow is gradually steady in the initial angular position of 15°. And this measurement condition is maintained for one minute to record the variations of FP cavity lengths and calculate the average values to analyze the wind pressure. Then, we adjust the aerodynamic THP to other angular positions with a step of 1° for measurement in the same way as above. As shown in Figure 8A, the FP cavity length of the 1st fiber-tip sensor corresponding to Port 1 in the sensor array decreases throughout the whole calibration process in a yaw angular range from 15° to −15° at each Mach number environment, the one corresponding to Port 2 keeps almost stable, while the one corresponding to Port 3 keeps increasing. The wind pressure introduced through the three ports of the aerodynamic THP (P_1, P_2, and P_3) can be obtained in real time by substituting the measured FP cavity lengths into the pressure calibration equation of the sensor array based on Equation 17. The average values of port pressure are shown in Figures 8B–8D. Until the free jet is terminated, the three cavity lengths of the fiber-tip sensors can be restored to the original state, indicating that the sensing diaphragm remains within the elastic deformation range. The total and static pressures (P_0, P_s) in the free jet are monitored in real time by its own measuring and control devices of the wind tunnel.

Through the aforementioned calibration process, P_1, P_2, P_3, P_0, and P_s are all acquired in the flow fields of 0.2 Ma, 0.5 Ma, and 0.8 Ma with a yaw angular range of ±15°. The yaw angle coefficient K_β, total pressure coefficient K_0, and static pressure coefficients K_{13}, KK_1, and KK_3 are gained by substituting the above pressure values into Equations 8–12, respectively. These five calibration coefficients follow a certain rule with the changes of yaw angles. The calibration maps of the related coefficients with angle variations in the range of ±15° are illustrated in Figure 9. K_β can be regarded as varying linearly with yaw angles in the testing angular range, as shown in Figure 9A. The other calibration coefficients exhibit nonlinear trends concerning yaw angle variations. The calibration curves of K_0 versus yaw angles can be fitted with quartic polynomial, as shown in Figure 9B.

Calibration curves of K_{13}, KK_1, and KK_3 are plotted in Figures 9C and 9D. It is worth mentioning that in order to minimize the calculation error, the three static pressure coefficients are employed simultaneously. With a
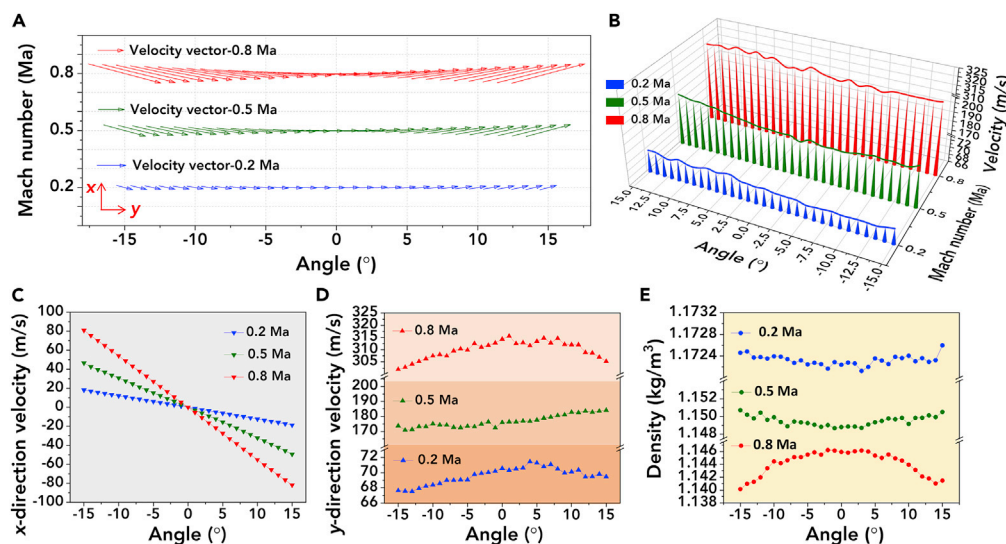
Figure 10. The flow characteristics in the airflow field environments of 0.2 Ma, 0.5 Ma, and 0.8 Ma at yaw angles of $\pm 15°$ inferred from the three-port pressure values of the fiber-optic integrated aerodynamic THP during the calibration process

(A) The velocity vectors.
(B) The velocity magnitudes.
(C) The velocity magnitudes in the x-direction.
(D) The velocity magnitudes in the y-direction.
(E) Densities of the airflow.

relatively small airflow yaw angle ($\beta \leq \pm 5°$), the differential pressure between P_1 and P_3 may be quite small. Because Port 1 and Port 3 are placed symmetrically with respect to Port 2, the pressures introduced and measured from Port 1 and Port 3 are very approximate at this point. A slight inaccuracy in the measured P_1 and P_3 will result in an amplification of the error in the static pressure value calculated from K_{13}, as indicated in Equation 10. Similarly, it will appear that Port 1 and Port 2 have a small pressure difference within $-15° \leq \beta < -5°$, while the situation is analogous for Port 2 and Port 3 in the yaw angle measurement range of $5° < \beta \leq 15°$. The inversion procedure of the static pressure using KK_1 and KK_3, which may bring amplified errors, is also not suitable in the above two yaw angular ranges, as indicated in Equations 11 and 12. Therefore, the calibration curves of K_{13} is commonly adopted for the above yaw angular measurement range of $-15° \leq \beta < -5$ and $5° < \beta \leq 15°$. The calibration curves of KK_1 and KK_3 are both employed to obtain the static pressure values separately when the yaw angle is in the range of $\beta \leq \pm 5°$, and then the average of the two is considered the accurate static pressure.

The calibration maps can be interpolated in preparation for acquiring the characteristics of velocity vector, total pressure, static pressure, and density of the flow field using the developed fiber-optic integrated aerodynamic THP. Because the total and static pressure of the free jet have been already monitored during the experimental calibration process, we demonstrate the velocity vector and density of the airflow using the derivation procedure mentioned in the previous section based on Equations 8–16. Figure 10A depicts the velocity vectors in the airflow field environments of 0.2 Ma, 0.5 Ma, and 0.8 Ma at yaw angles of $\pm 15°$ inferred from the three-port pressure values (P_1, P_2, and P_3) of the fiber-optic integrated aerodynamic THP during the calibration process. The flow velocity direction changes with the rotation of the aerodynamic THP in each flow field state and the velocity magnitudes increase with the increased Mach numbers. Also as shown in Figure 10B, the velocity magnitude at each yaw angle is maintained within a modest variation interval and fluctuates up and down at approximately 70.5 m/s, 179.0 m/s, and 313.8 m/s, respectively. This fluctuation may be generated by the inherent instability of the airflow provided by the air compressor. In addition, an increase in wind pressure supplied by the air compressor is always accompanied by an increase in instability, which results in more dramatic fluctuations in higher Mach numbers.

Based on the description in Figure 1B, the measured velocity vectors can be decomposed in a 2D right-angle coordinate system. The velocity magnitudes on the axes of x and y are shown in Figures 10C and 10D. In different flow field environments, the velocity magnitude in x-direction all decreases with yaw angle variations in the angular range from $-15°$ to $0°$, as shown in Figure 10C. Until the pressure ports of the fiber-optic integrated aerodynamic THP are facing the free-jet streamline at a yaw angle of $0°$, the velocities reach 0. In the angular range from $0°$ to $15°$, the velocity direction changes, and the magnitude increases with the increasing angle until the velocity magnitude peaks at an angle of $15°$. The intervals of x-direction velocity magnitude variations are 18.1∼−18.6 m/s, 46.6∼−49.3 m/s, and 80.9∼−81.8 m/s at Mach numbers of 0.2 Ma, 0.5 Ma, and 0.8 Ma, respectively. The magnitude of the velocity in the y-direction also fluctuates with the changes of yaw angles in each Mach number environment, as shown in Figure 10D. The fluctuations are over and under 69.6 m/s, 176.8 m/s, and 310.0 m/s, respectively. Figure 10E shows the airflow density variations inferred from Equation 16 during the calibration process, ranging from 1.1721 to 1.1726 kg/m^3, 1.1487 to 1.1507 kg/m^3, and 1.1402 to 1.1462 kg/m^3, corresponding to 0.2 Ma, 0.5 Ma, and 0.8 Ma environments, respectively.

### Velocity vector testing in unknown flow fields

Generally, calibration maps for a certain flow field environment or angular range are employed for measurement in the corresponding range. In 0.2 Ma, 0.5 Ma, and 0.8 Ma flow fields with yaw angles of $\pm15°$, the airflow velocities at the measurement points are controlled by the air compressor and the yaw angles are generated through randomly rotating the developed fiber-optic integrated aerodynamic THP by the 3-axis rotary stage, as shown in Figure 6. At this time, the monitored atmospheric pressure P_a of the experimental environment is 100.43 kPa, and the corresponding total temperatures T_0 of the three airflow fields with the above Mach numbers are 28.9°C, 30.6°C, and 32.6°C, respectively. Real-time pressure data at each test point are acquired by the developed fiber-optic integrated aerodynamic THP and the self-developed multichannel WLI interrogator as P_1, P_2, and P_3 in unknown airflow fields that do not exceed the calibration range. Then, the three detected pressures are substituted into the aforementioned dimensionless calibration coefficient equations based on Equations 8–12. Compared them with the interpolated calibration maps to find the total pressure, static pressure, yaw angle, velocity magnitude, 2D velocity decomposition, and airflow density at the measurement points. Figure 11A describes the 18 groups of pressure readings from the developed fiber-optic integrated aerodynamic THP in the testing flow fields of 0.2 Ma, 0.5 Ma, and 0.8 Ma with different yaw angles. Through the calculation based on the calibration maps mentioned above, the magnitude and direction of the airstream velocity are deduced. The output velocity vectors in the unknown flow fields are shown in Figure 11B.

The measured velocity magnitude, x-direction velocity, y-direction velocity, total pressure, static pressure, and density of the unknown airflow field are output through the aforementioned calculation method and depicted in Figure 12. The velocity magnitudes of the six measured points in each Mach number environment at different yaw angles are shown in Figure 12A. The yaw angles are learned and the velocity magnitudes are all consistent with the airflow environment at each Mach number conditions of 0.2 Ma, 0.5 Ma, and 0.8 Ma. The velocity magnitudes fluctuate up and down at approximately 70.8 m/s, 181.2 m/s, and
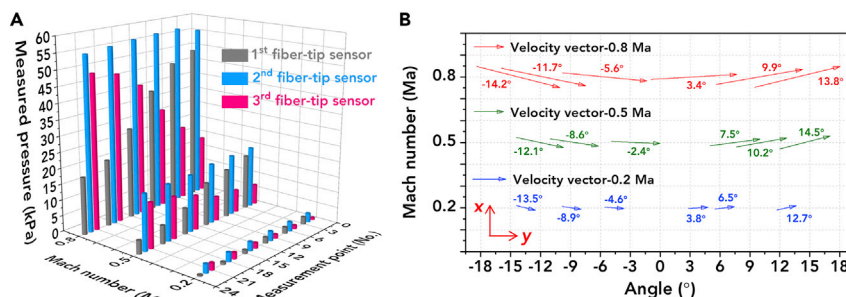
Figure 11. Pressure readings from the fiber-optic integrated aerodynamic THP and the measured velocity vectors in the testing flow fields of 0.2 Ma, 0.5 Ma, and 0.8 Ma with different yaw angles
(A) 18 groups of pressure readings.
(B) The measured velocity vectors.
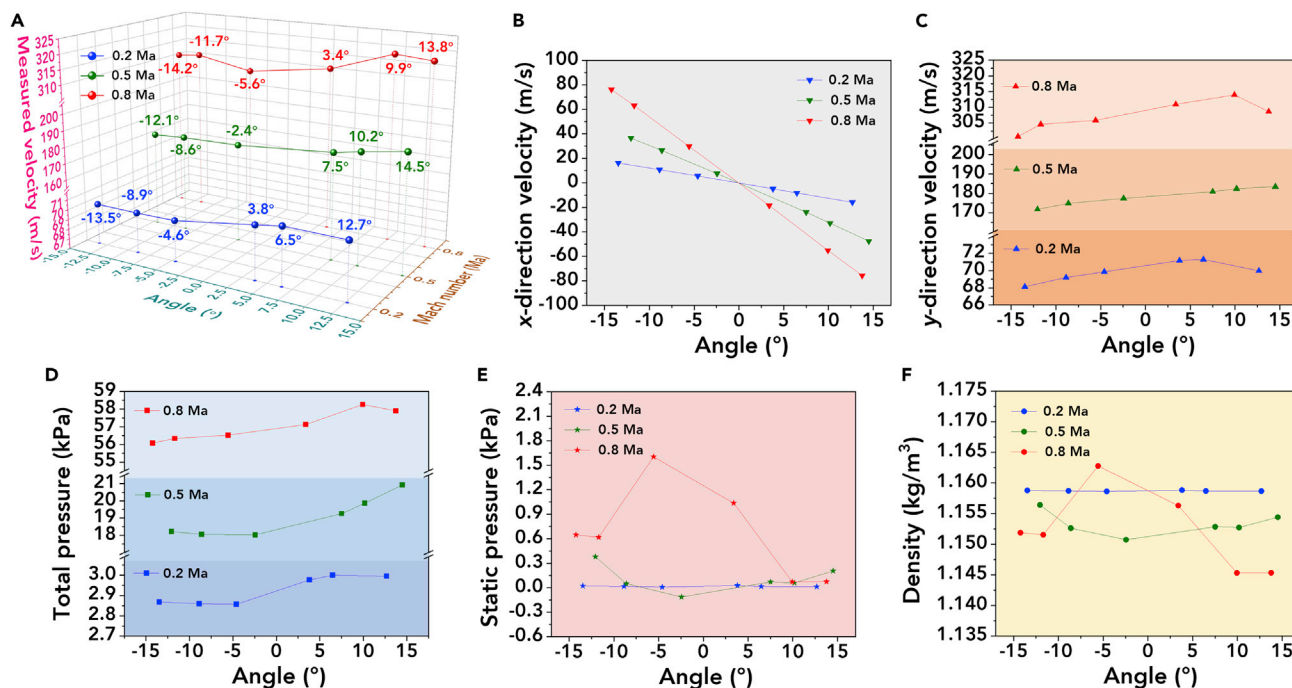
Figure 12. The deduced flow characteristics of the unknown airflow field
(A) The measured velocity magnitude.
(B) *x*-direction velocity.
(C) *y*-direction velocity.
(D) Total pressure.
(E) Static pressure.
(F) Airflow density.

312.8 m/s in the yaw range of $-13.5°$–$12.7°$, $-12.1°$–$14.5°$, and $-14.2°$–$13.8°$, respectively. The analysis of the velocity components in the *x* and *y* direction is described in Figures 12B and 12C. The variation pattern of the *x*-direction components along the yaw angle is similar to that of the calibration process, as shown in Figures 10C and 12B. With the changes in yaw angle, the velocity variations in the *x*-direction range from 16.3 to -15.7 m/s, 36.7 to -47.5 m/s, and 76.3 to -75.6 m/s, respectively. The velocities first decrease until they are 0, after which the directions of the velocities are all deflected and the velocity magnitudes increase again. The *y*-direction velocity components are also output in Figure 12C, where the velocity magnitude varies over and under 69.9 m/s, 178.5 m/s, and 307.5 m/s, respectively.

The inferred total pressure and static pressure are depicted in Figures 12D and 12E, both of which do not fluctuate greatly with the measurement angles. As the airflow velocity in the wind tunnel increases, more dramatic fluctuations in total and static pressure occur. This is a result of the increased wind pressure supplied by the air compressor and the consequently increased instability. The density values of these measurement points are also described in Figure 12F, showing density varying ranges of 1.1586–1.1588 kg/m^3, 1.1508–1.1564 kg/m^3, and 1.14536–1.1628 kg/m^3 at 0.2 Ma, 0.5 Ma, and 0.8 Ma flow environments, respectively. Through the entire testing, the developed aerodynamic THP shows no noticeable degradation or malfunction, indicating that the integrated fiber-optic tip pressure sensor array can operate effectively even at high Mach numbers. And the developed fiber-optic integrated aerodynamic THP is desired to offer some application values in future turbomachinery investigations.

Conclusions

In summary, a fiber-optic integrated aerodynamic THP for high-velocity vector measurements is proposed and experimentally demonstrated in wind tunnel testing. The integrated sensor array consists of three MEMS diaphragm-based fiber-optic tip pressure sensors. They are encapsulated in three pressure conduits near the probe ports to mitigate pneumatic pressure loss and explore flow characteristics more reliably. The

miniaturization of the aerodynamic THP reduces the perturbation to the airflow field and facilitates the reconstruction of the flow field vectors. The aerodynamic THP is properly calibrated in a subsonic free-jet wind tunnel at different Mach numbers of 0.2 Ma, 0.5 Ma, and 0.8 Ma with a flow angle interval of 1° in the angle varying range of ±15°. The calibration and measurement data of the aerodynamic THP are acquired in real time by the compact self-developed multichannel WLI interrogator that mainly works on the principle of precise and fast scanning of an MG-Y tunable laser. And the plotted calibration maps have helped to reconstruct the velocity vectors in unknown flow fields while understanding related flow characteristics. The fiber-optic integrated aerodynamic THP benefits from the miniaturized probe head and the compact fast-scanning system, which is expected to become a new option for turbomachinery research in the future.

Limitations of the study

Our work focuses on the design and development of a fiber-optic integrated aerodynamic THP and a compact self-developed multichannel WLI interrogator. The feasibility of this fiber-optic WLI sensing system for high-velocity vector and related flow characteristic measurements in a subsonic free-jet wind tunnel is experimentally demonstrated. However, practical investigations on some aerodynamic issues, including compressor cascade performance, propeller blade flow, horseshoe vortices, etc., still require further research using this fiber-optic WLI sensing system in the future.

STAR★METHODS

Detailed methods are provided in the online version of this paper and include the following:

- KEY RESOURCES TABLE
- RESOURCE AVAILABILITY
  - Lead contact
  - Materials availability
  - Data and code availability
- EXPERIMENTAL MODEL AND SUBJECT DETAILS
- METHOD DETAILS
  - Sensing diaphragm preparation
  - Fiber-optic WLI sensing system
  - Pressure ports arrangement of the aerodynamic THP
  - Yaw angular measurement range
- QUANTIFICATION AND STATISTICAL ANALYSIS

AUTHOR CONTRIBUTIONS

Conceptualization, Z.J. and Y.L.; methodology, Y.L. and Z.J.; software, Q.L. and A.L.; investigation, Y.L., W.L., S.Z., and A.L.; writing–original draft, Y.L.; writing–review & editing, Z.J. and W.P.; funding acquisition, W.P. and Z.J.; resources, W.P., F.T., and R.L.; supervision, W.P. and Z.J.

DECLARATION OF INTERESTS

The authors have no relevant financial interests in this article and no potential conflicts of interest to disclose.

REFERENCES

Andersen, B.W., and Binder, R.C. (1967). The analysis and design of pneumatic systems. J. Appl. Mech. *34*, 1055. https://doi.org/10.1115/1.3607835.

Anderson, J.D. (2010). Fundamentals of Aerodynamics (Tata McGraw-Hill Education).

Argüelles Díaz, K.M., Fernández Oro, J.M., and Blanco Marigorta, E. (2009). Cylindrical three-hole pressure probe calibration for large angular range. Flow Meas. Instrum. *20*, 57–68. https://doi.org/10.1016/j.flowmeasinst.2008.12.001.

Argüelles Díaz, K.M., Fernández Oro, J.M., and Blanco Marigorta, E. (2008a). Extended angular range of a three-hole cobra pressure probe for incompressible flow. ASME. J. Fluids Eng. *130*, 101401. https://doi.org/10.1115/1.2969457.

Argüelles Díaz, K.M., Oro, J.M.F., and Marigorta, E.B. (2008b). Direct calibration framework of triple-hole pressure probes for incompressible flow. Meas. Sci. Technol. *19*, 075401. https://doi.org/10.1088/0957-0233/19/7/075401.

Argüelles Díaz, K.M., Fernández Oro, J.M., Blanco Marigorta, E., and Barrio Perotti, R. (2010). Head geometry effects on pneumatic three-hole pressure probes for wide angular range. Flow Meas. Instrum. *21*, 330–339. https://doi.org/10.1016/j.flowmeasinst.2010.04.004.

Azartash-Namin, S.K. (2017). Evaluation of Low-Cost Multi-Hole Probes for Atmospheric Boundary Layer Investigation (Master's dissertation, Oklahoma State University). https://www.proquest.com/docview/2036894293?pq-origsite=gscholar&fromopenview=true.

Backman, D.G., and Williams, J.C. (1992). Advanced materials for aircraft engine applications. Science *255*, 1082–1087. https://doi.org/10.1126/science.255.5048.1082.

Bai, H., Li, S., Barreiros, J., Tu, Y., Pollock, C.R., and Shepherd, R.F. (2020). Stretchable distributed fiber-optic sensors. Science *370*, 848–852. https://doi.org/10.1126/science.aba5504.

Bailey, S.C.C., Kunkel, G.J., Hultmark, M., Vallikivi, M., Hill, J.P., Meyer, K., Tsay, C., Arnold, C., and Smits, A. (2010). Turbulence measurements using a nanoscale thermal anemometry probe. J. Fluid Mech. *663*, 160–179. https://doi.org/10.1017/S0022112010003447.

Beer, W. (2008). Optimisation of a Compound Lean Turbine Blade in a Linear Cascade (Dissertation). https://publik.tuwien.ac.at/files/PubDat_167302.pdf.

Cipullo, A., Gruca, G., Heeck, K., De Filippis, F., Iannuzzi, D., Minardo, A., and Zeni, L. (2012). Numerical study of a ferrule-top cantilever optical fiber sensor for wind-tunnel applications and comparison with experimental results. Sens. Actuator A. Phys. *178*, 17–25. https://doi.org/10.1016/j.sna.2012.01.044.

Crowder, J., Watzlavick, R., and Krutckoff, T. (1997). Airplane Flow-Field Measurements (World Aviation Congress (ARC)). https://arc.aiaa.org/doi/pdf/10.2514/6.1997-5535.

Díaz, D.L. (2003). Experimental Calibration of Three-Hole Pressure Probes With Different Head Geometries. Diploma Thesis (Vienna University of Technology). https://publik.tuwien.ac.at/files/pub-mb_1582.pdf.

Fujiwara, E., da Silva Delfino, T., Destri Cabral, T., and de Barros Cordeiro, C.M. (2020). All-optical fiber anemometer based on the pitot-static tube. IEEE Trans. Instrum. Meas. *69*, 1805–1811. https://doi.org/10.1109/TIM.2019.2915392.

Giovanni, D. (1982). Flat and Corrugated Diaphragm Design Handbook (Marcel Dekker).

Gossweiler, C.R., Kupferschmied, P., and Gyarmathy, G. (1995). On fast-response probes: Part 1—technology, calibration, and application to turbomachinery. J. Turbomach. *117*, 611–617. https://doi.org/10.1115/1.2836579.

Han, M., Zhang, Y., Shen, F., Pickrell, G.R., and Wang, A. (2004). Signal-processing algorithm for white-light optical fiber extrinsic Fabry–Perot interferometric sensors. Opt. Lett. *29*, 1736–1738. https://doi.org/10.1364/OL.29.001736.

Heckmeier, F.M., Iglesias, D., Kreft, S., Kienitz, S., and Breitsamter, C. (2019). Development of unsteady multi-hole pressure probes based on fiber-optic pressure sensors. Eng. Res. Express *1*, 025023. https://doi.org/10.1088/2631-8695/ab4f0d.

Jing, Z. (2006). Study on White Light Extrinsic Fabry-Perot Interferometric Optical Fiber Sensor and its Application (Doctoral dissertation, Dalian University of Technology). https://oversea.cnki.net/KCMS/detail/detail.aspx?dbcode=CDFD&dbname=CDFD9908&filename=2006146437.nh&uniplatform=OVERSEAS_EN&v=YYx56hq2F7Ph7waZrz1PhXgtRBeB-Mf51XgV-UvsowZyJ84oy8NXjOAYfDYACCQ6.

Jing, Z., Liu, Y., Zhang, Y., Li, A., Song, P., Wu, Z., Zhang, Y., and Peng, W. (2018). Highly Sensitive FBG-FP Sensor For Simultaneous Measurement of Humidity and Temperature. In 26th International Conference on Optical Fiber Sensors (OSA). https://doi.org/10.1364/ofs.2018.wf79.

Johansen, E.S., Allen, R.D., and Rediniotis, O.K. (2003). Embedded-sensor, fast-response multi-hole probes. In 41st Aerospace Sciences Meeting and Exhibit (AIAA). https://doi.org/10.2514/6.2003-1091.

Lawson, N.J., Correia, R., James, S.W., Partridge, M., Staines, S.E., Gautrey, J.E., Garry, K.P., Holt, J.C., and Tatam, R.P. (2016). Development and application of optical fibre strain and pressure sensors for in-flight measurements. Meas. Sci. Technol. *27*, 104001. https://doi.org/10.1088/0957-0233/27/10/104001.

Li, Q., Xu, J., Maeda, T., Kamada, Y., Nishimura, S., Wu, G., and Cai, C. (2019). Laser Doppler Velocimetry (LDV) measurements of airfoil surface flow on a Horizontal Axis Wind Turbine in boundary layer. Energy *183*, 341–357. https://doi.org/10.1016/j.energy.2019.06.150.

Liu, G., Sheng, Q., Hou, W., and Han, M. (2016). Optical fiber vector flow sensor based on a silicon Fabry–Perot interferometer array. Opt. Lett. *41*,

4629–4632. https://doi.org/10.1364/OL.41.004629.

Liu, Q., Jing, Z., Liu, Y., Li, A., Xia, Z., and Peng, W. (2019). Multiplexing fiber-optic Fabry–Perot acoustic sensors using self-calibrating wavelength shifting interferometry. Opt. Express *27*, 38191–38203. https://doi.org/10.1364/OE.381197.

Liu, Q., Li, A., Liu, Y., Jing, Z., and Peng, W. (2021). TWDM-assisted active quadrature demodulation of fiber-optic fabry–perot acoustic sensor network. J. Lightwave Technol. *39*, 3991–3997. https://doi.org/10.1109/JLT.2020.3043024.

Liu, Y., Jing, Z., Li, R., Zhang, Y., Liu, Q., Li, A., Zhang, C., and Peng, W. (2020a). Miniature fiber-optic tip pressure sensor assembled by hydroxide catalysis bonding technology. Opt. Express *28*, 948–958. https://doi.org/10.1364/OE.380589.

Liu, Y., Jing, Z., Liu, Q., Li, A., Teng, C.a., Cheung, Y., Lee, A., Tian, F., and Peng, W. (2020b). Differential-pressure fiber-optic airflow sensor for wind tunnel testing. Opt. Express *28*, 25101–25113. https://doi.org/10.1364/OE.401677.

Mersinligil, M., Brouckaert, J.F., and Desset, J. (2011). Unsteady pressure measurements with a fast response cooled probe in high temperature gas turbine environments. J. Eng. Gas Turb. Power *133*, 081603. https://doi.org/10.1115/1.4002276.

Mousavi, A., and Hoseinibalam, F. (2020). Optical counting of guided particles in a vortex beam as an optical tube by laser-two-focus method. Flow Meas. Instrum. *73*, 101745. https://doi.org/10.1016/j.flowmeasinst.2020.101745.

O'Connor, S., Bernacil, M.A., and Derickson, D. (2008). Generation of high speed, linear wavelength sweeps using sampled grating distributed Bragg reflector lasers. In LEOS 2008-21st Annual Meeting of the IEEE Lasers and Electro-Optics Society (IEEE), pp. 147–148. https://doi.org/10.1109/LEOS.2008.4688531.

Pask, J.A., and Fulrath, R.M. (1962). Fundamentals of glass-to-metal bonding: VIII, nature of wetting and adherence. J. Am. Ceram. Soc. *45*, 592–596. https://doi.org/10.1111/j.1151-2916.1962.tb11067.x.

Pisasale, A.J., and Ahmed, N.A. (2002). A novel method for extending the calibration range of five-hole probe for highly three-dimensional flows. Flow Meas. Instrum. *13*, 23–30. https://doi.org/10.1016/s0955-5986(02)00011-0.

Ragni, D., van Oudheusden, B.W., and Scarano, F. (2011). Non-intrusive aerodynamic loads analysis of an aircraft propeller blade. Exp. Fluids *51*, 361–371. https://doi.org/10.1007/s00348-011-1057-7.

Rautenberg, A., Allgeier, J., Jung, S., and Bange, J. (2019). Calibration procedure and accuracy of wind and turbulence measurements with five-hole probes on fixed-wing unmanned aircraft in the atmospheric boundary layer and wind turbine wakes. Atmosphere *10*, 124. https://doi.org/10.3390/atmos10030124.

Roux, J. (2004). Experimental Investigation of Nozzle Guide Vanes in a Sector of an Annular

Cascade. Doctoral Dissertation (KTH Royal Institute of Technology). http://kth.diva-portal.org/smash/record.jsf?pid=diva2.

Royce, R. (2015). The Jet Engine (John Wiley & Sons).

Schettini, F., Rito, G.D., and Galatolo, R. (2018). Smart air-data probe for fault-tolerant flow measurements. In 2018 5th IEEE international workshop on metrology for aeroSpace (MetroAeroSpace) (IEEE), pp. 602–607. https://doi.org/10.1109/MetroAeroSpace.2018.8453555.

Soto-Valle, R., Bartholomay, S., Alber, J., Manolesos, M., Nayeri, C.N., and Paschereit, C.O. (2020). Determination of the angle of attack on a research wind turbine rotor blade using surface pressure measurements. Wind Energ. Sci. *5*, 1771–1792. https://doi.org/10.5194/wes-5-1771-2020.

Telionis, D., Yang, Y., and Rediniotis, O. (2009). Recent developments in multihole probe (MHP) technology. In 20th international congress of mechanical engineering (ABCM). http://abcm.org.br/anais/cobem/2009/pdf/COB09-3415.pdf.

Teng, C. (2021). Mechanism Investigation on the Effect of Wake Shape on Flow of High-Load Low-Pressure turbine. Master's Dissertation (Dalian University of Technology). https://doi.org/10.26991/d.cnki.gdllu.2021.001687.

Tropea, C., Yarin, A., and Foss, J.F. (2007). Handbook of Experimental Fluid Mechanics (Springer). https://doi.org/10.1007/978-3-540-30299-5.

Uzol, O., and Katz, J. (2007). Flow Measurement Techniques in Turbomachinery (Springer). https://doi.org/10.1007/978-3-540-30299-5_14.

Wang, C., Zhang, X., Jiang, J., Liu, K., Wang, S., Wang, R., Li, Y., and Liu, T. (2019). Fiber optical temperature compensated anemometer based on dual Fabry-Perot sensors with sealed cavity. Opt. Express *27*, 18157–18168. https://doi.org/10.1364/OE.27.018157.

Wang, G.F., Duchaine, F., Papadogiannis, D., Duran, I., Moreau, S., Gicquel, L.Y., and Gicquela, L.Y.M. (2014). An overset grid method for large eddy simulation of turbomachinery stages. J. Comput. Phys. *274*, 333–355. https://doi.org/10.1016/j.jcp.2014.06.006.

Wang, W., Jiang, X., and Yu, Q. (2012). Temperature self-compensation fiber-optic pressure sensor based on fiber Bragg grating and Fabry-Perot interference multiplexing. Opt. Commun. *285*, 3466–3470. https://doi.org/10.1016/j.optcom.2012.04.001.

Wang, W., Wu, N., Tian, Y., Niezrecki, C., and Wang, X. (2010). Miniature all-silica optical fiber pressure sensor with an ultrathin uniform diaphragm. Opt. Express *18*, 9006–9014. https://doi.org/10.1364/OE.18.009006.

Westerweel, J., Elsinga, G.E., and Adrian, R.J. (2013). Particle image velocimetry for complex and turbulent flows. Annu. Rev. Fluid Mech. *45*, 409–436. https://doi.org/10.1146/annurev-fluid-120710-101204.

White, F.M. (2011). Fluid Mechanics (In SI Units) (Mcgraw Hill Higher Education).

Wyler, J.S. (1975). Probe blockage effects in free jets and closed tunnels. ASME J. Eng. Power *97*, 509–514. https://doi.org/10.1115/1.3446046.

Xie, J., Wang, F., Pan, Y., Wang, J., Hu, Z., and Hu, Y. (2015). High resolution signal-processing method for extrinsic Fabry–Perot interferometric sensors. Opt. Fiber Technol. *22*, 1–6. https://doi.org/10.1016/j.yofte.2014.11.010.

Zachos, P.K., Grech, N., Charnley, B., Pachidis, V., and Singh, R. (2011). Experimental and numerical investigation of a compressor cascade at highly negative incidence. Eng. Appl. Comp. Fluid *5*, 26–36. https://doi.org/10.1080/19942060.2011.11015350.

Zhou, H., and Sheplak, M. (2020). A MEMS-based fast-response miniature five-hole probe with optical pressure transducers. J. Microelectromech. Syst. *29*, 960–965. https://doi.org/10.1109/JMEMS.2020.3009927.

Zhou, X., Yu, Q., and Peng, W. (2019). Fiber-optic Fabry-Perot pressure sensor for down-hole application. Opt. Lasers Eng. *121*, 289–299. https://doi.org/10.1016/j.optlaseng.2019.04.028.

Zou, M., Liao, C., Liu, S., Xiong, C., Zhao, C., Zhao, J., Gan, Z., Chen, Y., Yang, K., Liu, D., et al. (2021). Fiber-tip polymer clamped-beam probe for high-sensitivity nanoforce measurements. Light Sci. Appl. *10*, 171. https://doi.org/10.1038/s41377-021-00611-9.

STAR★METHODS

KEY RESOURCES TABLE

REAGENT or RESOURCE	SOURCE	IDENTIFIER
Chemicals, peptides, and recombinant proteins		
Iodine	Aladdin	CAS: 7553-56-2
Potassium iodide	Aladdin	CAS: 7681-11-0
Deposited data		
Raw and analyzed data	This paper	https://doi.org/10.17632/4vmp97dd6f.1
Software and algorithms		
Code for data acquisition and analysis	This paper	https://doi.org/10.17632/4vmp97dd6f.1
Cross-correlation WLI signal processing Method	Jing (2006)	https://oversea.cnki.net/KCMS/detail/detail.aspx?dbcode = CDFD&dbname = CDFD9908&filename = 2006146437.nh&uni-platform = OVERSEAS_EN&v = YYx56hq2F7Ph7waZrz1PhXgtRBeB-Mf51XgV-UvsowZyJ84oy8NXjOAYfDYACCQ6
Other		
Photoresist	Shipley	S1805
MG-Y tunable laser	AOC Technologies	http://en.hubei.gov.cn/business/enterprises/201605/t20160517_834543.shtml

RESOURCE AVAILABILITY

Lead contact

Further information and requests for resources and reagents should be directed to and will be fulfilled by the lead contact, Zhenguo Jing (jingzg@dlut.edu.cn).

Materials availability

This study did not generate new unique reagents.

Data and code availability

- Data generated in this study have been deposited at Mendeley Data (https://doi.org/10.17632/4vmp97dd6f.1).

- Code for data acquisition and analysis in this work is publicly available at Mendeley Data (https://doi.org/10.17632/4vmp97dd6f.1).

- Any additional information required to reanalyze the data reported in this paper is available from the lead contact upon request.

EXPERIMENTAL MODEL AND SUBJECT DETAILS

This study does not use experimental models typical in the life science.

METHOD DETAILS

Sensing diaphragm preparation

The metallic diaphragms are manufactured by magnetron sputtering and MEMS technology. Magnetron sputtering we employed allows precise control of the gold diaphragms' thickness over a wide range, enabling the construction of thinner sensing diaphragms and higher sensor sensitivity for our wind tunnel research demands. Combined with MEMS manufacturing process, the high uniformity of the prepared gold sensing diaphragms is also a key factor in supporting simultaneous and consistent response as well as good repeatability of the three fiber-tip sensors. This is very important for the stable operation and

measurement reliability of the aerodynamic THP in practical velocity vector and related flow field characteristics studies. In MEMS manufacturing process, we use positive photoresist (S1805, Shipley) for photolithography, followed by wet etching using a mixture of iodine, potassium iodide, and DI water in a mass ratio of 1:5:100 (I_2:KI:H_2O) to form the shape of gold sensing diaphragms. The entire MEMS manufacturing process is clean and efficient, producing hundreds of well-shaped diaphragms at a time.

Fiber-optic WLI sensing system

Our work can be summarized as including two aspects of research, one is the design and fabrication of fiber-optic integrated aerodynamic THP, and the other is the development of a multi-channel WLI interrogator (an acquisition and demodulation system). And this fiber-optic sensing system is successfully applied in a subsonic free-jet wind tunnel. Our designed fiber-optic integrated aerodynamic THP is an intrusive device that offers measurements of free-jet flow fields, yielding velocity vectors and other related flow characteristics. Accurate measurement of flow field parameters usually requires minimizing flow disturbances created by the intrusive probes. Miniature ultra-thin circular gold diaphragms manufactured from MEMS technology form the basic pressure sensing units of the fiber-tip sensors in the fiber-optic integrated aerodynamic THP, while helping to create miniature sensing structures with an outer diameter of just ~125 μm. The smaller sizes of the single fiber-tip sensors benefit the miniaturization of the aerodynamic THP top area, thereby reducing intrusive perturbation to the testing airflow field and facilitating the exploration of actual flow characteristics. The high uniformity of the gold sensing diaphragms produced by the MEMS manufacturing process is also a key factor in supporting the simultaneous and consistent response as well as stable operation of the three fiber-tip sensors in practical free-jet velocity vector and flow field characteristics application studies.

The fast real-time data from the fiber-optic integrated aerodynamic THP is acquired by our self-developed compact multi-channel WLI interrogator consisting of an MG-Y tunable laser (AOC Technologies), an FPGA control and acquisition module, and three photodetectors. Full-spectrum wavelength scanning of the MG-Y laser at an interval of 8 pm from 1527 nm to 1567 nm and synchronized data acquisition with a frequency of 100 Hz can be both implemented by our multi-channel WLI interrogator. The output spectra are simultaneously processed by the cross-correlation WLI signal processing method (Jing, 2006), and the demodulated lengths of the three FP cavities are then expressed as functions of applied wind pressure. Combining the unique advantages of the fiber-optic tip pressure sensor array and the compact fast-scanning system, this work is desired to provide a potential candidate for turbomachinery experimental investigation in the fluid mechanics community.

Pressure ports arrangement of the aerodynamic THP

Aerodynamic THP is often made up of a streamlined axisymmetric body pointing to the airflow and used for 2D flow fields analysis. Unlike the well-known Pitot tube with separate measurement ports for total and static pressure, any points on the tip of a THP may capture the total pressure at a certain yaw angle (Tropea et al., 2007). The surface pressure of the THP tip is usually sampled at three points to determine the direction and magnitude of the 2D flow field. Through experimental and empirical analysis, and long-term evolution in the field of aerodynamics, the three locations are typically designed on the axis of the probe tip and at two equally spaced points on both sides of the probe tip surface (Argüelles Díaz et al., 2010; Díaz, 2003). This design is based on the following measurement principles. When the flow velocity vector is perpendicular to the central pressure port on the probe tip surface, that point gives the conventional stagnation/total pressure. The yaw direction can be inferred by relating the differential pressure between the symmetrical pressure side ports to the inflow velocity vector through proper calibration (Argüelles Díaz et al., 2009, 2010; Díaz, 2003). The fiber-tip sensors in this work are installed in accordance with the distribution of the pressure ports on the aerodynamic THP to measure the values of inflow pressure. The calibration method and subsequent data processing approach for the aerodynamic THP are also designed according to the central and symmetrical ports for reliable experimental results.

Yaw angular measurement range

From some literature reports as well as our previous measurement experience and demands in general flow fields, the angular measurement ranges of −15°–15° of THP can already be applied to some typical turbomachinery studies, such as turbine rotor blades, horseshoe vortices, and turbine cascades, etc (Soto-Valle et al., 2020; Mersinligil et al., 2011; Beer, 2008; Teng, 2021). Therefore, within this angular range of −15°–15°, the feasibility of the fiber-optic integrated aerodynamic THP and multi-channel WLI interrogator for

flow field calibration and velocity vector measurements was verified. While this fiber-optic sensing system has the ability to increase the measurement range by improving the pneumatic parameters of the THP and calibration procedures to fit other particular airflows. On the one hand, the capacities of the measurement device depend not only on the performance of the sensors but also on the aerodynamic properties of the THP. By changing some parameters of the THP, their aerodynamic properties can be well adjusted to extend the angular range of measurements (Argüelles Díaz et al., 2008a, 2010). On the other hand, such limitations also arise from the current experimental calibration conditions of the aerodynamic THP. By optimizing the calibration conditions, the measurement range can be improved (Pisasale and Ahmed, 2002; Argüelles Díaz et al., 2008b). At this stage, the main goal of successfully applying this fiber-optic WLI sensing system to 2D velocity vector measurements and related flow characteristics analysis in a free-jet wind tunnel has been achieved. In the next stage, we will make some improvements depending on the demands to enhance their applicability. And we hope that this fiber-optic WLI sensing system will provide a new option for applications in turbomachinery studies in the future.

QUANTIFICATION AND STATISTICAL ANALYSIS

This study does not include quantification and statistical analysis.